*Acta Cryst.* (1992). A**48**, 626-639

# Determination of the Dispersive Correction $f'(E)$ to the Atomic Form Factor from X-ray Reflection

By F. Stanglmeier, B. Lengeler and W. Weber

*Institut für Festkörperforschung, Forschungszentrum Jülich, Postfach* 1913, *D*-5170 *Jülich, Germany*

and H. Göbel and M. Schuster

*Siemens AG, Zentrale Forschung und Entwicklung, Otto-Hahn-Ring* 6, *D*-8000 *München* 83, *Germany*

(*Received* 22 *February* 1991; *accepted* 6 *March* 1992)

## Abstract

It is shown in this paper that the reflectivity of X-rays at smooth and flat surfaces gives the dispersive correction $f'(E)$ to the atomic form factor with an accuracy comparable to that obtained by X-ray interferometry. A detailed set of values of $f'(E)$ in the energy range 7-27 keV is given for Ni, Cu, CuO, Ta, $LiTaO_3$, Pt and Au, together with the corresponding linear absorption coefficients $\mu/\rho$. Whenever comparison is possible the values of $f'(E)$ agree very well with those obtained by interferometry or by Kramers-Kronig transformation. Data calculated according to Cromer & Liberman [*J. Chem. Phys.* (1970). **53**, 1891-1898] agree well with our data far from absorption edges. At the edges there are substantial differences because the calculations do not take into account the structure of the edges, their chemical shift in compounds and the EXAFS structure above the edges. Below absorption edges the values of $f'(E)$ for metals and their oxides are equal, provided the chemical shift in the position of the edges is taken care of. This feature is interesting in anomalous scattering experiments, where the variation of $f'$ with energy is used to vary the scattering contrast of a given atomic species. Once $f'(E)$ is known, X-ray reflectivity measurements can be used to determine the density and the thickness of layers on flat substrates. In addition, the roughness of the air-layer and layer-substrate interfaces have been determined with high precision in the metals and oxides mentioned above.

## 1. Introduction

The atomic form factor $f$ is the factor by which the scattering amplitude of X-rays scattered by an atom is increased compared to that scattered by a single free electron (Compton & Allison, 1935; James, 1967):

$$f = f_0 + f' + if''. \tag{1}$$

At energies far above the absorption edges $f$ is given by $f_0$, which decreases in a characteristic way with increasing scattering angle. In the forward-scattering direction $f_0$ is equal to the atomic number $Z$. In this case, all the electrons constructively contribute to the scattering amplitude. In the vicinity of the absorption edges, energy-dependent corrections $f'(E)$ and $f''(E)$ must be taken into account. $f''(E)$ is proportional to the coefficient of linear absorption $\mu(E)$, which has been tabulated for all atoms in the X-ray energy range (Veigele, 1974). The dispersive correction $f'(E)$ is related to the change in phase velocity when X-rays enter into matter. The corrections $f' + if''$ are needed in X-ray structure analysis and especially in contrast variation (Stuhrmann, 1981). The most important methods for determining $f'(E)$ are interferometry developed by Bonse & Hart (1965) and the calculation from $\mu(E)$ by means of a Kramers-Kronig relation. Interferometry is probably the most accurate method for $f'(E)$ measurements, but in general it has only been applied to a restricted energy range around absorption edges (Bonse & Hart, 1966; Siddons & Hart, 1983; Bonse & Hartmann-Lotsch, 1986; Begum, Hart, Lea & Siddons, 1986). The Kramers-Kronig calculations are hampered by systematic errors, since $\mu(E)$ must be known over a wide energy range extending to many MeV (Fukamachi, Hosoya, Kawamura, Hunter & Nakano, 1978; Kawamura & Fukamachi, 1978; Dreier, Rabe, Malzfeldt & Niemann, 1984). Cromer & Libermann (1970) and Cromer (1983), using relativistic Hartree-Fock wave functions, have calculated $f'(E)$ for a number of systems.* These calculations do not take into account the fine structure in X-ray absorption and the shift of the edge position with the valency of the absorbing species.

Another method for the determination of $f'(E)$, which has been known for many years, is the total reflection of X-rays from flat surfaces (Kiessig, 1931; Compton & Allison, 1935; Parratt & Hempstead, 1954; James, 1967; Fukamachi *et al.*, 1978; Vineyard, 1982). To our knowledge, up to now no high-quality

* Note that we have used the same experimental energy levels as Cromer (1983) for the position of the edges, which we obtained from Burr (1974).

0108-7673/92/040626-14$06.00 © 1992 International Union of Crystallography

data have been obtained with this method. The purpose of this paper is to show that this method can provide high-quality results, comparable in accuracy to those obtained by interferometry. Values of $f'(E)$ have been obtained in a wide energy range from 7 to 27 keV for Ni, Cu, CuO, Ta, $LiTaO_3$, Pt and Au. The measurements were performed at the storage ring DORIS at Hasylab, Hamburg. It is necessary to use flat and smooth samples of large size (typically 10 cm in diameter). The surface roughness has to be taken into account in the data analysis. The most serious source of systematic errors are errors in the absolute value of the angle of X-ray incidence. Therefore a spectrometer has been built that allows an accuracy of 0.001° in this angle to be obtained. Reflectivity measurements over four decades are easily achieved with this set-up.

## 2. Total reflection of X-rays

X-rays are refracted according to Snell's law,

$$n_1 \cos \theta_1 = n_2 \cos \theta_2 \tag{2}$$

when crossing an interface between two media with indices of refraction $n_1$ and $n_2$ (Fig. 1). In condensed matter the index of refraction for hard X-rays in the 10 keV range is slightly smaller than 1. It can be written as (James, 1967)

$$n = 1 - (N_a r_0 / 2\pi)\lambda^2 \sum_j (\rho_j / A_j) f_j, \tag{3}$$

where $\lambda = hc/E$ is the photon wavelength, $E$ the photon energy, $N_a$ the Avogrado constant, $r_0 = 2.818 \times 10^{-5}$ Å the classical electron radius, $\rho_j$ the mass density and $A_j$ the atomic mass of the $j$th constituent. The atomic form factor $f$ being complex [(1)], $n$ can be written as

$$n = 1 - \delta - i\beta, \tag{4}$$

where

$$\delta = (N_a r_0 / 2\pi)\lambda^2 \sum_j (\rho_j / A_j)(Z_j + f'_j), \tag{5}$$

$$\beta = \mu\lambda / 4\pi. \tag{6}$$

Inserting appropriate values into (5) and (6) shows that $\delta$ and $\beta$ are positive and of the order $10^{-5}$ to

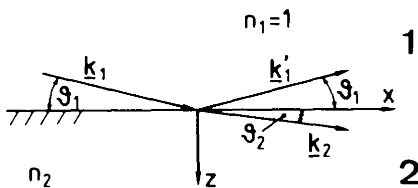


Fig. 1. Refraction and reflection of X-rays at an interface between a vacuum ($n_1 = 1$) and a medium with index of refraction $n_2$.

$10^{-7}$. Since $n$ is slightly smaller than 1, the X-rays are refracted away from the normal when entering matter, as indicated in Fig. 1. Therefore $\theta_2$ will become zero at a finite value $\theta_{1c}$ of $\theta_1$. Below this angle of incidence, total external reflection will occur. When the absorption is neglected ($\beta_2 = 0$), $\theta_{1c}$ is given by

$$\theta_{1c} = (2\delta_2)^{1/2} = \left\{ (N_a r_0 / \pi) \sum_j (\rho_j / A_j)(Z_j + f'_j) \right\}^{1/2} \lambda. \tag{7}$$

The critical angle is proportional to the square root of the mass density, to the square root of $(Z + f')$ and to the photon wavelength $\lambda$. Inserting appropriate values in (7) shows that the angle of total reflection for hard X-rays in condensed matter in the 10 keV range is below about 0.5°. This justifies why $f_0$ can be replaced in (5) by $Z$. In reality, absorption can never be neglected. It smears out the reflectivity curve in the range of $\theta_{1c}$. Therefore $f'(E)$ can only be obtained if the measured reflectivity is fitted in a large angular range to the Fresnel reflectivity. In addition, the surface roughness has to be taken into account.

Firstly, we will give the result for the reflected and transmitted intensities at a flat interface without roughness (Born & Wolf, 1965; Jackson, 1975). The **E** and **B** vectors of the incoming wave are

$$\mathbf{E}_1 = \mathbf{A}_1 \exp[i(\mathbf{k}_1 \cdot \mathbf{r} - \omega t)] \quad \text{and} \quad \mathbf{B}_1 = n_1 \hat{\mathbf{k}}_1 \times \mathbf{E}_1 \tag{8}$$

where $\hat{\mathbf{k}}_1$ denotes a unit vector in the direction of $\mathbf{k}_1$. The corresponding reflected fields are indicated by a prime and the transmitted fields by an index 2, since they propagate in medium 2.

$$\mathbf{E}_2 = \mathbf{A}_2 \exp[i(\mathbf{k}_2 \cdot \mathbf{r} - \omega t)] \quad \text{and} \quad \mathbf{B}_2 = n_2 \hat{\mathbf{k}}_2 \times \mathbf{E}_2 \tag{9}$$

$$\mathbf{E}'_1 = \mathbf{A}'_1 \exp[i(\mathbf{k}'_1 \cdot \mathbf{r} - \omega t)] \quad \text{and} \quad \mathbf{B}'_1 = n_1 \hat{\mathbf{k}}'_1 \times \mathbf{E}'_1. \tag{10}$$

At the interface $z = 0$ between media 1 and 2 the tangential components of the resulting **E** and **B** fields must be continuous. This leads to the Fresnel equations for the reflected and transmitted amplitudes and intensities. Since we are only concerned with small angles (below 1°), we can approximate $\sin \theta$ and $\tan \theta$ by $\theta$. In this case, $s$- and $p$-polarized waves give the same result, so that we will confine ourselves to $s$ polarization, in which $\mathbf{A}_i$ and $\mathbf{A}'_i$ have only a $y$ component ($i = 1, 2$) (see Fig. 1). The continuity of **E** and **B** gives

$$\frac{A'_1}{A_1} = \frac{\theta_1 - \theta_2}{\theta_1 + \theta_2} \equiv r_{12} \quad \text{and} \quad \frac{A_2}{A_1} = \frac{2\theta_1}{\theta_1 + \theta_2} \equiv t_{12} \tag{11}$$

and

$$\mathbf{k}_1 = k_1 \begin{pmatrix} 1 \\ 0 \\ \theta_1 \end{pmatrix}, \quad \mathbf{k}'_1 = k_1 \begin{pmatrix} 1 \\ 0 \\ -\theta_1 \end{pmatrix}, \quad \mathbf{k}_2 = k_1 \begin{pmatrix} 1 \\ 0 \\ \theta_2 \end{pmatrix}. \tag{12}$$

The reflectivity $R$ and the transmissivity $T$ are given by

$$R=|A_1'/A_1|^2 \quad \text{and} \quad T=|A_2/A_1|^2. \tag{13}$$

Energy conservation requires

$$|r_{12}|^2+|t_{12}|^2[\mathrm{Re}\,(\theta_2)]/\theta_1=1. \tag{14}$$

In addition, the amplitudes (11) fulfil the condition

$$r_{12}^2+t_{12}t_{21}=1. \tag{15}$$

From the refraction law, $\cos\theta_1=n_2\cos\theta_2$, it follows for small angles that

$$\theta_2=(\theta_1^2-2\delta_2-2i\beta_2)^{1/2}\equiv p_2+iq_2 \tag{16}$$

so $\theta_2$ is complex. The real and imaginary parts are given by the relations

$$\begin{aligned}2p_2^2&=[(\theta_1^2-2\delta_2)^2+4\beta_2^2]^{1/2}+(\theta_1^2-2\delta_2),\\ 2q_2^2&=[(\theta_1^2-2\delta_2)^2+4\beta_2^2]^{1/2}-(\theta_1^2-2\delta_2).\end{aligned} \tag{17}$$

$p_2/\theta_{1c}$ and $q_2/\theta_{1c}$ are given in Fig. 2 as a function of the normalized incident angle $\theta_1/\theta_{1c}$. Without absorption, $p_2$ is zero below $\theta_{1c}$ and tends towards $\theta_1$ for large values of $\theta_1$, whereas $q_2$ is zero above $\theta_{1c}$ in this case. This means that $\theta_2$ is purely imaginary below and real above $\theta_{1c}$. The absorption makes $\theta_2$ complex everywhere and smooths out the sharp variation of $p_2$ and $q_2$ at $\theta_{1c}$. The transmitted amplitude $E_2$ is

$$\mathbf{E}_2=\mathbf{A}_2\exp[i(k_1x+k_1p_2z)-i\omega t]\exp(-k_1q_2z). \tag{18}$$

It is exponentially damped with a decay constant

$$\begin{aligned}z_0&=(k_1q_2)^{-1}\\ &=\lambda 2^{-1/2}\{[(\theta_1^2-2\delta_2)^2+4\beta_2^2]^{1/2}-(\theta_1^2-2\delta_2)\}^{-1/2}.\end{aligned} \tag{19}$$

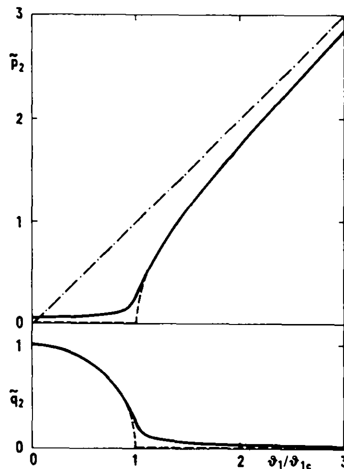


Fig. 2. Normalized real and imaginary parts $\tilde{p}_2=p_2/\theta_{1c}$ and $\tilde{q}_2=q_2/\theta_{1c}$ of $\theta_2=p_2+iq_2$ vs the normalized angle of incidence $\theta_1/\theta_{1c}$ for metallic Ta at 9.800 keV. The dashed curves apply to zero absorption.

For illustration $z_0$ is given for metallic tantalum in Fig. 3. Above the critical angle the absorption determines the penetration depth. On top of the white line at the $L_3$ edge of Ta (9.880 keV) the penetration depth is appreciably smaller than below the edge at 9.850 keV. Below the angle of total reflection the penetration depth becomes more and more independent on $\lambda$ and tends towards

$$z_{00}=(2\pi)^{-1}\{\pi A/[N_a r_0\rho(Z+f')]\}^{1/2} \quad \text{for} \quad \theta_1\to 0. \tag{20}$$

$z_{00}$ depends on the mass density and ranges from 64 Å in Si ($\rho=2.33\ \mathrm{g\,cm^{-3}}$) to 23 Å in Pt ($21.4\ \mathrm{g\,cm^{-3}}$). In the range of total reflection all X-ray techniques (such as absorption, diffraction, fluorescence analysis, topography *etc.*) become surface sensitive, in the sense that the signal originates in a 20 to 70 Å thick layer below the surface (Eisenberger & Marra, 1981; Vineyard, 1982).

The reflectivity of X-rays from a smooth flat surface is given by (13),

$$R=\left|\frac{A_1'}{A_1}\right|^2=\frac{(\theta_1-p_2)^2+q_2^2}{(\theta_1+p_2)^2+q_2^2}. \tag{21}$$

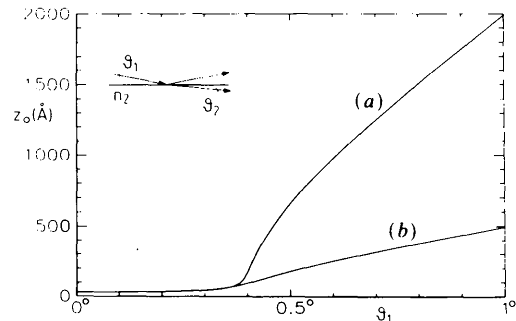


Fig. 3. Penetration depth $z_0$ of the transmitted electric field $E_2$ ($1/e$ attenuation length) in metallic Ta at ($a$) 9.850 and ($b$) 9.880 keV. This is just below the Ta $L_3$ edge and on top of the white line at that edge.

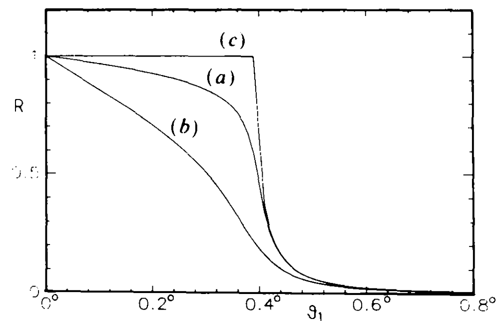


Fig. 4. Reflectivity of X-rays from a flat metallic Ta surface without surface roughness. ($c$) Without absorption, $R$ is 1 for $\theta_1$ below $\theta_{1c}$. Absorption drastically reduces the reflectivity at and below $\theta_{1c}$ [($a$) 9.850 keV and ($b$) 9.880 keV].

Without absorption $R$ becomes 1 below $\theta_{1c}$ and drops to zero for $\theta_1 \geq 1.5\ \theta_{1c}$ according to

$$R \simeq \delta_2^2/(4\theta_1^4). \tag{22}$$

The absorption drastically reduces the reflectivity below $\theta_{1c}$ as shown in Fig. 4 for Ta. The figure shows very clearly that it is not possible to determine the value of $\theta_{1c}$ from a reflectivity measurement in a simple way. It is necessary to fit the whole curve to an expression like (21). In addition, it turns out that surface roughness has to be taken into account to obtain accurate values of $f'(E)$. Appropriate expressions will be derived in the next section.

### 3. Reflectivity from multiple layers including interface roughness

We consider $N$ layers with thickness $d_j$ and index of refraction $n_j$. When interface roughness is weak (below 50 Å) we can apply the following model. The rough surface is replaced by a set of flat surfaces that are distributed according to a Gaussian around the average interface (Fig. 5). Since the surfaces in the set are assumed to be flat and parallel to one another and to the plane $z=0$, this model does not include diffuse scattering. Therefore it is only applicable when the roughness is weak. We consider two interfaces limiting the layer $j$. One of the surfaces of the set that is displaced by $u_j$ from the average surface is shown in Fig. 5 The coordinate $z_j$ of each layer refers to the middle of that layer. The interfaces are located at $-d_j/2+u_{j-1}$ and $+d_j/2+u_j$ with $u_j$ distributed according to a Gaussian

$$w(u_j) = (2\pi\sigma_j^2)^{-1/2} \exp(-u_j^2/2\sigma_j^2). \tag{23}$$

Since we will limit ourselves to small angles of incidence, we will only consider $s$ polarization. Denoting incoming waves without and reflected waves with a prime the electric field vectors in the $j$th layer read

$$\mathbf{E}_j(\mathbf{r}, t) = \begin{pmatrix} 0 \\ A_j \\ 0 \end{pmatrix} \exp[i(k_1 x + k_1\theta_j z_j - \omega t)]$$
$$\mathbf{E}'_j(\mathbf{r}, t) = \begin{pmatrix} 0 \\ A'_j \\ 0 \end{pmatrix} \exp[i(k_1 x - k_1\theta_j z_j - \omega t)]. \tag{24}$$

The **B** vectors follow from (8). Since

$$A_j(\text{in } j\text{th layer at interface } j) = A_j \exp(ik_1\theta_j d_j/2), \tag{25}$$

the continuity of the tangential components of **E** and **B** give a relation between the amplitudes in the $j$th and $(j+1)$th layers that is, in matrix formulation,

$$\begin{bmatrix} A_j \\ A'_j \end{bmatrix} = R^{j,j+1} \begin{bmatrix} A_{j+1} \\ A'_{j+1} \end{bmatrix} \tag{26}$$

with

$$R_{\mu\nu}^{j,j+1} = [\theta_j + (-1)^{\mu-\nu}\theta_{j+1}]/2\theta_j \times \exp\{i(k_1/2)[(-1)^{\mu}\theta_j d_j + (-1)^{\nu}\theta_{j+1}d_{j+1}]\} \times \exp\{ik_1 u_j[(-1)^{\mu}\theta_j - (-1)^{\nu}\theta_{j+1}]\}, \tag{27}$$

where $\mu$, $\nu = 1, 2$. The different models based on the Gaussian distribution, which have been treated in the literature, differ by the way in which the average over $u_j$ is carried out.

*(a) One interface*

Layer 1 is the vacuum or air with $n_1 = 1$ and layer 2, with refractive index $n_2$, is infinitely thick, so that there is no reflected amplitude, *i.e.* $A'_2 = 0$. Then

$$A'_1/A_1 = R_{21}^{12}/R_{11}^{12}. \tag{28}$$

(i) When amplitudes are superposed with their corresponding phases, the reflected amplitude is given by

$$A'_1/A_1 = (\theta_1 - \theta_2)/(\theta_1 + \theta_2) \exp(ik_1\theta_1 d_1) \times \exp(2ik_1\theta_1 u_1). \tag{29}$$

The Gaussian average denoted by $\langle\cdots\rangle$ gives

$$(2\pi\sigma_j^2)^{-1/2} \int_{-\infty}^{\infty} du_j \exp[\pm ik_1(\theta_j \pm \theta_{j+1})u_j - u_j^2/2\sigma_j^2] = \exp[-\tfrac{1}{2}k_1^2(\theta_j \pm \theta_{j+1})^2\sigma_j^2] \tag{30}$$

so that

$$\langle (A'_1/A_1)\exp(-ik_1\theta_1 d_1)\rangle = r_{12}\exp(-2k_1^2\theta_1^2\sigma_1^2). \tag{31}$$

The reflectivity in this case is

$$R = |r_{12}|^2 \exp(-4k_1^2\theta_1^2\sigma_1^2). \tag{32}$$

This is the well known Gaussian damping given by Rayleigh (see Beckmann & Spizzichino, 1963). It is the most widely used roughness correction to the Fresnel reflectivity $|r_{12}|^2$, although it does not describe well the measured reflectivities of X-rays (see below).

(ii) Another approach is to average the individual matrix coefficients $R_{\mu\nu}^{12}$ in (28).

$$\langle A'_1/A_1\rangle = \langle R_{21}^{12}\rangle/\langle R_{11}^{12}\rangle. \tag{33}$$

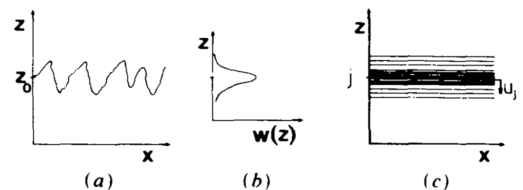


Fig. 5. Slight roughness (*a*) is described by a set of flat surfaces (*c*) distributed around the average surface according to a Gaussian (*b*) with standard deviation $\sigma$. The surfaces are displaced by $u_j$ from the average interface $j$.

This leads by means of (30) to

$$\langle (A_1'/A_1)\exp(-ik_1\theta_1 d_1)\rangle = r_{12}\exp(-2k_1^2\theta_1\theta_2\sigma_1^2) \quad (34)$$

and

$$R = |r_{12}|^2 \exp(-4k_1^2\theta_1 p_2\sigma_1^2). \quad (35)$$

This expression differs from (32) by $\theta_1^2$ being replaced by $\theta_1 p_2$. As shown in Fig. 2 the two expressions are identical well above $\theta_{1c}$. However, they differ dramatically in the vicinity of $\theta_{1c}$. Since $p_2$ is much smaller than $\theta_1$ at $\theta_{1c}$, (35) strongly suppresses the influence of the surface roughness around $\theta_{1c}$. It turns out that (35) describes the measured reflectivity of X-rays much better than does (32). This is shown in Fig. 6, in which the reflectivity of 7.200 keV photons from a 1000 Å gold film on a 4 in Si wafer are fitted with (32) and (35). Experimental details are given below. It is obvious that the Rayleigh version does not fit the data in the vicinity of the critical angle whereas (35) fits the data well in the whole angular range. The Au film has a roughness $\sigma_1 = 13$ Å, which corresponds to a full width at half-maximum of 31 Å. The roughness of this same sample was probed with a scanning tunneling microscope. The surface turned out to be covered with neighboring rounded knobs of about 400 Å basal diameter and about 40 Å in height.

Equation (35) was first obtained by Nevot & Croce (1980) and later by Sinha, Sirota, Garoff & Stanley (1988). They used different approaches from the one described here. Equation (35) describes the experimental results in an adequate way, whereas (32) does not. It must be concluded that the coherency of the X-ray wave at the rough interface is lost: the incoming and the reflected amplitudes each suffer a phase randomization, independent of one another. The resulting averaged amplitudes superpose to give the reflected intensity. This is what (33) expresses.

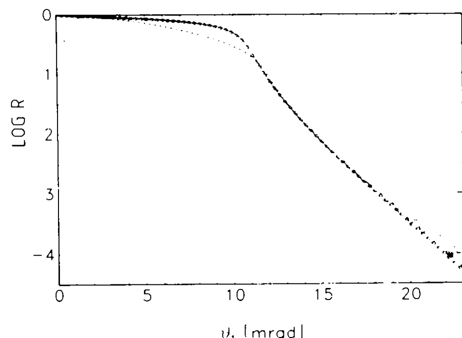


Fig. 6. Reflectivity of 7.200 keV photons from a 1000 Å thick Au layer on a 4 in Si wafer (——). The result is fitted with the expressions (32) (+) and (35) (∘). It is obvious that (35) fits the data very well in the whole angular range. In both fits it was assumed that the Au layer is infinitely thick, therefore the thickness oscillations are not reproduced.

(*b*) *Three interfaces*

We will now treat the case of two layers on a substrate. $j = 2$ and 3 are the layers and $j = 4$ is the substrate. When the substrate is very thick, $A_4' = 0$. By repeatedly using (26), $A_1'/A_1$ may be expressed in terms of the $R_{\mu\nu}^{j,j+1}$, where $\mu$, $\nu = 1, 2$. Each individual matrix coefficient will be averaged according to (30). The result is

$$R = |\langle A_1'/A_2\rangle|^2 = \left|\frac{\hat r_{12} + \hat r_{23}\gamma_2 + \hat r_{34}\gamma_2\gamma_3 + \hat r_{12}\hat r_{23}\hat r_{34}\gamma_3}{1 + \hat r_{12}\hat r_{23}\gamma_2 + \hat r_{23}\hat r_{34}\gamma_3 + \hat r_{12}\hat r_{34}\gamma_2\gamma_3}\right|^2 \quad (36)$$

with

$$\hat r_{j,j+1} = (\theta_j - \theta_{j+1})/(\theta_j + \theta_{j+1})\exp(-2k_1^2\sigma_j^2\theta_j\theta_{j+1}) \quad (37)$$

$$\gamma_j = \exp(2ik_1\theta_j d_j). \quad (38)$$

Each reflected amplitude $\hat r_{j,j+1}$ at the interface $j$ is reduced by an exponential as in (34) with a factor $\theta_j\theta_{j+1}$ instead of $\theta_j^2$. The factors $\gamma_j$ take care of the phase shift and absorption suffered by a wave when passing down and up again through the $j$th layer. They give rise to oscillations in the reflectivity above the critical angle as shown below in Fig. 11 for an Au layer on an Si wafer. An expansion of the denominator in (36) gives a geometrical series in powers of $r_{12}$, $r_{23}$ and $r_{34}$, which can be interpreted as a superposition of multiple reflections from the different interfaces. It is easy to recover some special cases from (36). $\sigma_j = 0$ ($j = 1, 2, 3$) gives the reflectivity from layers without roughness. The reflectivity from one layer on a substrate is obtained when $\gamma_3 = 0$. Of course, (35) for a very thick layer is recovered when $\gamma_2$ and $\gamma_3$ are made zero.

There is a second model that shows how roughness can be treated in reflectivity. Instead of describing the roughness by a Gaussian smearing with a standard deviation as in (35), the roughness can be treated as an additional layer of reduced density and of a certain thickness. For example, the reflectivity from a rough substrate may be modeled by (36) with $\sigma_j = 0$ and $\gamma_3 = 0$, *i.e.* a layer on a substrate with two smooth interfaces ($\sigma_1 = \sigma_2 = 0$). The roughness is then characterized by a layer of thickness $d_2$ and density $\rho_2$. $Z$ and $f'$ are chosen to be identical to those of the substrate. This procedure turns out to be adequate for low roughness *i.e.* small $d_2$. Examples of these two treatments of roughness are given below.

## 4. Experimental details

The experimental set-up used to determine the energy dependence of $f'$ is installed at the beam line RÖMO I at Hasylab in Hamburg. A schematic view is given in Fig. 7. The white beam from the storage ring DORIS passes through slit 1 of height 0.8 mm and width 12 mm before it falls on a double-crystal

monochromator. We have used Si(111) below 8 keV and Si(311) crystals above that energy. At 3.7 GeV electron energy and a current of 100 mA about $10^9$ photons $s^{-1}$ pass the monochromator at 10 keV in a 1.5 eV wide energy band. The ionization chamber 0 in Fig. 7 provides an input for the piezoelectric feedback system which keeps the transmission through the monochromator at a fixed percentage of the maximum transmission (Krolzig, Materlik, Swars & Zegenhagen, 1984). The main purpose of this system is to reject harmonics from the transmitted beam. The rejection of the third harmonic of an 8 keV beam is better than 1 part in $10^4$ as estimated from the $K$ edge of a Pd foil (Pd $K$ edge at 24.3 keV) that was placed in the 8.2 keV beam. Slit 2 has a height of 75 μm. For wafers with a diameter of 10 cm, which were almost always used in this investigation, the area illuminated by the beam is smaller than 10 cm for angles $\theta_1$ exceeding 0.043°.

The samples are mounted on a goniometer that has angular and translational freedom of movement (Fig. 8). The angle of incidence $\theta_1$ is computer controlled by the goniometer $\theta_1$ with an accuracy of 0.0001°. The axis of rotation of this goniometer is 170 mm above its top level. The height adjustment $z_2$ allows one to locate the surface of the sample within ±50 μm in the axis of rotation of $\theta_1$. This axis of rotation and the beam of width 12 mm are set parallel to one another by means of the goniometer rotation $\rho$. The translation $z_1$ is needed to make the beam, the axis of rotation $\theta_1$ and the sample surface coincide. Sometimes Bragg peaks from single-crystal samples may hamper the measurements. They can be eliminated by means of the goniometer rotation $\psi$ whose axis is perpendicular to the sample. The detector arm rotation $\theta_1'$ is computer controlled and can be moved independently of $\theta_1$ or in such a way that $\theta_1' = 2\theta_1$. A slit system 3 in front of the detector with variable width is needed for separating specular and diffuse scattering from the sample (Fig. 7).

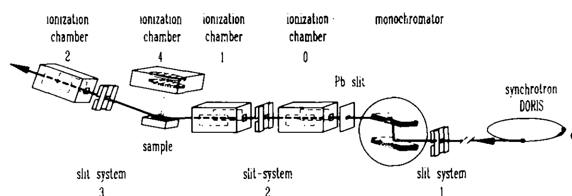


Fig. 7. Diagram of the set-up used to determine $f'(E)$ from total reflection. The reflected intensity is measured by detector 2. The fluorescence emitted by the sample is detected by detector 4.

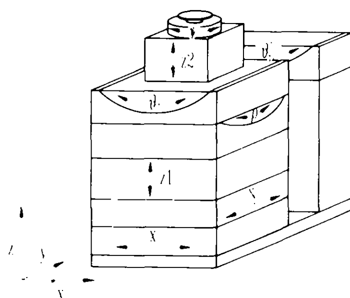

Fig. 8. Goniometer with the different degrees of freedom used to position the sample in the beam and to control the angle of incidence $\theta_1$ and of reflection $\theta_1'$. The synchrotron light enters from the right.

The ionization chambers 1 and 2 measure the incident and reflected intensities. Chamber 4 located 3 cm above the sample with an opening of 15 cm measures the fluorescence emitted by the sample. This chamber is filled with krypton at $10^5$ Pa. Chambers 1 and 2 are filled with mixtures of nitrogen and argon so that they absorb 10% and about 95% of the incoming intensity, respectively.

The error in determining the angle of incidence $\theta_1$ is the main limitation to the accuracy with which $f'(E)$ can be determined by total reflection. The angular reproducibility of the goniometer angle $\theta_1$ in Fig. 8 is 0.0005°. The zero of angle has to be determined for each sample. Fig. 9 illustrates the principle of the calibration procedure. Images of the direct and reflected beams are recorded on a Polaroid film. For exposure to the direct beam the sample is lowered below the beam by means of stage $z_1$. The angle $\theta_1$ is given by 0.5 arctan $(d/D)$. For flat samples (wafer bow less than 10 μm) and for sharp reflections from the sample, an accuracy of 0.001° is obtained.

The output of the ionization chambers is converted into a voltage by means of Keithley amplifiers 427 or 18000-20. This voltage is converted into a frequency, which is measured with a Borer counter 1008 and stored by a MicroVAX computer. The whole detection system is linear over four decades when the Keithley amplifier 427 is used and over more than six decades when the Keithley amplifier 18000-20 is used (Storb, Dedek, Lengeler, Weber & Schuster, 1991). Great care must be taken to minimize offset drifts by shielding the electronic set-up and by avoiding strong temperature drifts.

The samples used in this investigation are listed in Table 1. Electron-gun evaporation was done in a vacuum of $10^{-4}$ Pa. The thickness homogeneity over the wafer is better than 1%. The copper oxide was

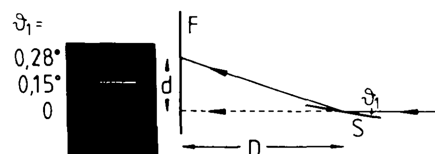


Fig. 9. Procedure for calibrating the zero of the angle $\theta_1$. Images of the direct beam and of the beam reflected by the sample $S$ (Au on Si) are recorded on a Polaroid film ($F$). The angle $\theta_1$ is given by $0.5\tan^{-1}(d/D)$. The precision is 0.001°.

Table 1. *Sample specifications*

| | | Layer thickness | Substrate | Deposited by |
|---|---|---|---|---|
| (i) | Au | 1000 Å | 4 in Si, 200 Å $SiO_2$, 200 Å Ti | Evaporation |
| (ii) | Pt | 1000 Å | 4 in Si, 200 Å Ti | Evaporation |
| | Pt | 3000 Å | 4 in Si | Evaporation |
| (iii) | $LiTaO_3$ | 500 μm | Single crystal, polished | |
| (iv) | Ta | 1000 Å | 4 in Si | Sputtering |
| | Ta | 3000 Å | 4 in Si | Evaporation |
| (v) | Cu | 1000 Å | 4 in Si, 200 Å Ti | Evaporation |
| (vi) | CuO | 2000 Å | 4 in Si, $Si_3N_4$ | Reactive sputtering |
| (vii) | Ni | 1000 Å | 4 in Si, 200 Å Ti | Evaporation |

deposited by reactive sputtering in an oxygen atmosphere of 0.16 Pa. An EXAFS scan in fluorescence at 0.15° (probing depth of about 40 Å) and at 0.5° (bulk material) showed the material to be CuO. The $LiTaO_3$ was a polished single-crystalline wafer of diameter 3 in. It had the lowest surface roughness of all samples.

The photographic detection of the reflected beam described above gives (besides the determination of the zero of $\theta_1$) a simple qualitative check of the sample quality. Fig. 9 shows a photograph of the direct beam and the beams reflected from Au on Si for the nominal positions $\theta_1 = 0.15$ and 0.28°. The reflected beams are almost as sharp as the direct beam. Samples with this type of reflection were found to be well suited for the $f'(E)$ measurements. The measured reflectivity can be fitted to a Fresnel-type expression [(36)] including surface roughness. On the other hand, the reflectivity from samples with broad reflections (1 mm or more) cannot be fitted to (36). Only samples with reflections like those in Fig. 9 were used for determining $f'(E)$.

A second criterion for the suitability of a sample was the amount of diffuse scattering. This is measured for à fixed angle $\theta_1$ by scanning the detector in the angular range around the totally reflected beam. In this mode of detection a slit 75 μm wide is positioned in front of detector 2 (slit 1 in front of detector 1 is also 75 μm wide). Fig. 10 shows the scans for two Ta layers, of thicknesses 1000 and 3000 Å (both deposited by electron-gun evaporation). $\theta_1$ was chosen to be 0.2, 0.3, 0.4, 0.45, 0.5, 0.6 and 0.7°. The angle of total reflection at 9.000 keV is 7.9 mrad (0.453°). The specularly reflected intensity shows up at $\theta_1' = \theta_1$. It sits on a background of diffuse scattering, which is more pronounced for the 3000 Å sample, indicating an increase of surface roughness with increasing sample thickness. It is noteworthy that the profile of the specular reflection sometimes increases with decreasing angle of incidence $\theta_1$. This is due to wafer bow and to the increasing length of the illuminated sample area with decreasing $\theta_1$. Therefore, the strategy for reflectivity measurement in the mode $\theta_1' = 2\theta_1$ was the following. To accept all of the specularly reflected beam a slit of width 500 μm, extending through an opening angle of 1.2 mrad, was installed in front of the detector. This angular width allows for some diffuse intensity to reach the detector. For the determination of $f'(E)$ we have used only samples in which the diffusive background below $\theta_{1c}$ was at least 3 orders of magnitude smaller than the specular reflectivity. Fig. 10 also shows the reflectivity $R(\theta_1)$ for the two samples. Curve ($b$) was measured with the slit in front of the detector opened by 1.2 mrad, whereas for curve ($a$) the slit was wide open (17.5 mrad). Samples, like the 1000 Å layer of Ta, for which curves ($a$) and ($b$) do not differ substantially, are well suited for $f'(E)$ measurements. On the other hand, samples like the 3000 Å layer of Ta, for which the reflectivities ($a$) and ($b$) differ dramatically above $\theta_{1c}$, were not used for the determination of $f'(E)$.

Evaporated Pt films showed a behavior similar to that of the Ta films. Pt samples of thickness 1000 Å were smooth and could be used for $f'(E)$ measurements, whereas Pt samples of 3000 Å in thickness were not appropriate.

The surface roughness of the samples used in this investigation was also measured by scanning electron and scanning force microscopy. The relationship between diffusive scattering and surface rougnness is the subject of a forthcoming publication (Weber & Lengeler, 1992).

Some of the samples (Ni, Cu and Ta) have a strong tendency to become covered with an oxide layer when in contact with air. X-ray absorption at grazing incidence is an ideal tool to detect the thickness and the chemical nature of these layers. Ni is covered by a 35 Å thick mixture of Ni and NiO. Cu is covered with about 35 Å of $Cu_2O$, whereas Ta is covered with

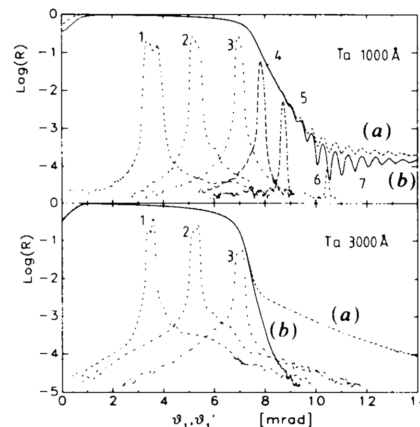


Fig. 10. Diffusive scattering from two Ta layers measured at 9.000 keV. The values $\theta_1$ were 0.2° (3.49 mrad) for curve 1, 0.3° (5.24 mrad) for curve 2, 0.4° (6.98 mrad) for curve 3, 0.45° (7.85 mrad) for curve 4, 0.5° (8.73 mrad) for curve 5, 0.6° (10.47 mrad) for curve 6 and 0.7° (12.22 mrad) for curve 7. The reflectivity curves ($a$) were measured with an open detector. The curves ($b$) were measured with an opening angle of 1.2 mrad so only the specular reflected intensity was allowed to reach the detector.

Table 2. *Energies of K and L edges in* eV (*Burr*, 1974)

| | Au | Pt | Ta | Cu | Ni |
|---|---|---|---|---|---|
| $K$ | | | | 8 980.6 | 8 331.65 |
| $L_1$ | 14 353.7 | 13 883 | 11 682 | | |
| $L_2$ | 13 736.1 | 13 272.3 | 11 132 | | |
| $L_3$ | 11 919.4 | 11 562 | 9 876.6 | | |

about 30 Å of $Ta_2O_5$. No oxides were detected on Au and Pt. The oxide layers were thin enough to be treated as a contribution to surface roughness.

### 5. Experimental results

In this section the reflectivity measurements made on the samples quoted in Table 1 will be described. The details of the data analysis are given for a few cases and the values of $f'(E)$ as well as of the absorption coefficients $\mu/\rho$ are given in tabulated form. The data were analyzed with the two models quoted above. Model 1 uses (36) with $\sigma_j \neq 0$ and the number of layers is equal to the number of layers deposited on the substrate. In this model the roughness of the interface $j$ enters into the damping factor as $\sigma_j^2\theta_j\theta_{j+1}$. Model 2 starts also from (36), but now with $\sigma_j = 0$ and the roughness is described by an additional thin layer.

(i) *Metallic* Au [*sample* (i) *in Table* 1]

Reflectivity measurements were made in the energy range from 7 to 27 keV. The first inflection points of the absorption edges are given in Table 2. The density of the Au film was chosen to be $19.32\,\text{g cm}^{-3}$ (Landolt-Börnstein, 1971). The analysis of the data was done in two ways. The plot of log $R$ *vs* $\theta_1$ emphasizes high-angle data.* Model 1 provided the best fit. The description of the data on a log $R$ scale is best suited when interface roughness is of primary concern. The plot of $R$ *vs* $\theta_1$ emphasized the reflectivity values below $\theta_{1c}$. Here, model 2 provided the best fit. The description of the data on the linear scale $R$ *vs* $\theta_1$ is most suitable when $f'(E)$ and density measurements are of primary interest. Fig. 11 shows reflectivity data at 11.501 keV (below the $L_3$ edge). Fig. 11($a$) shows the fit according to model 1 with Au on Ti. The finite thickness of the Ti layer does not show up in the data. The fit gives $f'(E) = -9.7$ (5) electrons, $\sigma_1 = 14$ (1) Å, $d_1(\text{Au}) = 1025$ (3) Å and $\sigma_2 = 10$ (2) Å. Fig. 11($b$) shows the fit of $R$ *vs* $\theta_1$ according to model 2. In this plot the Ti film is not visible at all and the Au film is characterized by two layers: an Au substrate covered with a thin film that describes the surface roughness. The fit gives $f'(E) = -9.5$ (5) electrons and $d_2 = 26$ (1) Å, $\rho_2 = 8$ (2) $\text{g cm}^{-3}$. The values $f'(E)$ obtained with both methods agree well within the margin of error. The error of ±0.5 electrons is mainly due to the error in the absolute value of the angle $\theta_1$ which is ±0.001°. Errors in the energy calibration and in the mass absorption coefficient $\mu/\rho$ can be neglected. If only high-quality samples are chosen and the slit width in front of detector 2 is chosen in such a way that only the specular reflected beam enters the detector, diffusive background does not contribute substantially to the error in $f'(E)$. The second largest source of error to $f'$ is the error in the density of the reflecting layer. In the present case of evaporated Au, the density was assumed to be that of bulk gold. A reduction of 1% in the density would increase $f'(E)$ at 11 keV by 0.7 electrons. The surface layer affected by roughness is $2.35 \times \sigma_1 = 33$ Å according to model 1 and 26 Å according to model 2, whereas the scanning tunneling microscope showed, for this Au sample, a structure with knobs of height about 40 Å. The agreement between the three values is reasonable, but it also shows that samples as smooth as possible should be selected for $f'(E)$ measurements.

* Throughout this paper log means logarithm to base 10.

Fig. 12 shows $f'(E)$ for Au in the energy range from 7 to 27 keV. The minima in $f'$ coincide with the first inflection point in $\mu/\rho$ at the absorption edges. The correction to the atomic form factor is substantial

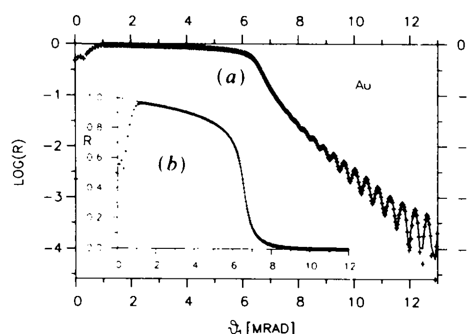


Fig. 11. Reflectivity (+) plotted for ($a$) log $R$ and ($b$) $R$ *vs* $\theta_1$ for the Au film (i) in Table 1 at 11.501 keV. Curve ($a$) is fitted with model 1 (——) and curve ($b$) with model 2 (——). The decrease in intensity below 1 mrad is due to the finite size of the sample.

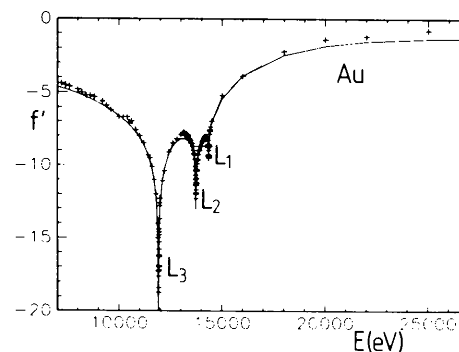


Fig. 12. Dispersive correction $f'(E)$ for metallic gold determined from total reflection of X-rays in the energy range from 7 to 27 keV (+). The data calculated according to Cromer & Liberman (1970) are given by the solid line.

in the whole energy range. For instance, at 11 923 keV a gold atom with $Z = 79$ behaves in diffraction like an atom with 60 instead of 79 electrons. Fig. 13 gives a comparison of our $f'(E)$ data with those given by Begum *et al.* (1986) from interferometry, with those determined by Dreier *et al.* (1984) from a Kramers-Kronig transformation and with those calculated according to Cromer & Liberman (1970). The overall agreement is satisfactory. Finally, we give in Table 3 the whole list of values of $f'(E)$ for metallic gold measured from total reflection. We give in the same list the values of $\mu/\rho$ measured with the same energy calibration. Transmission data have to be calibrated for the foil thickness and the energy-dependent sensitivity of the ionization chambers. This has been done by adjusting our data to the data of Veigele (1974) at common points on the energy scale. We feel that the juxtaposition of the data $f'(E)$ and $\mu/\rho$ is important for users of our $f'(E)$ data, since the absolute energy scale for the position of the absorption edges has errors of ±5 eV. Since it is easy to measure the absorption edge of gold, users can easily compare their energy scale to the one used in Table 3.

(ii) *Metallic* Pt [*sample* (ii) *in Table* 1]

The reflectivity was measured around the $L_3$ edge between 9 and 13 keV. We have assumed for the density the value $\rho = 21.47$ g cm$^{-3}$ (Landolt-Börnstein, 1971). The fits of the reflectivity were done with models 1 and 2. The results agree within ±0.2 electrons. The roughness affects a layer of 37 (3) Å at the surface, which has a density of 16.5 (5) g cm$^{-3}$. The values of $f'(E)$ are shown in Fig. 14 and given in Table 3 together with the values of $\mu/\rho$ determined in transmission at 77 K. Our data agree well with those calculated by Kramers-Kronig transformation (Dreier *et al.*, 1984) and also with those calculated by Cromer & Liberman (1970).

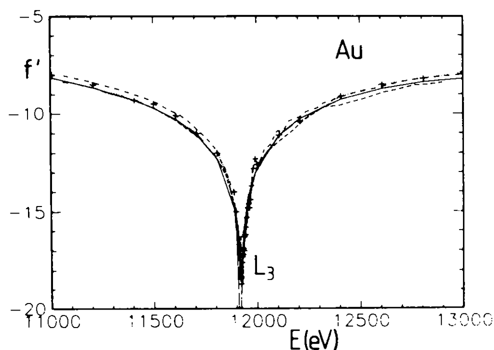


Fig. 13. Dispersive correction $f'(E)$ in the vicinity of the $L_3$ edge of metallic gold determined by total reflection of X-rays (+···+), by interferometry (- - -) (Begum *et al.*, 1986), by the Kramers-Kronig relation (-·--·-) (Dreier *et al.*, 1984) and by Cromer & Liberman (1970) (——).

(iii) *Single-crystal* $LiTaO_3$ [*sample* (iii) *in Table* 1]

The 3 in $LiTaO_3$ wafer had the smoothest surface of all samples. Reflectivity measurements were made between 8.8 and 20 keV. The density of $LiTaO_3$ is 7.45 g cm$^{-3}$ (Landolt-Börnstein, 1971). The dispersive correction for Li and O in this energy range is smaller than 0.1 electron and was neglected in the analysis. The values of $f'(E)$ for Ta in $LiTaO_3$ are given in Fig. 15. At the $L_3$ edge the correction is almost −30 electrons. The error is basically due to the error in $\theta_1$.

(iv) *Metallic* Ta [*sample* (iv) *in Table* 1]

In this sample, reflectivity data were collected around the $L_3$ edge between 9 and 11 keV. It is well known that sputtered Ta does not have a b.c.c. structure (it is X-ray amorphous) nor does it have the density of bulk tantalum which is 16.6 g cm$^{-3}$ (Landolt-Börnstein, 1971). Far away from the absorption edges we can expect $f'(E)$ to be equal for Ta and $LiTaO_3$. Using the values quoted in Table 3 for $LiTaO_3$, we first determined the density of our sputtered Ta film. It was 15.2 (3) g cm$^{-3}$, which is 8.5% less than the bulk density. The values of $f'(E)$ and $\mu/\rho$ determined by absorption at 77 K are given in

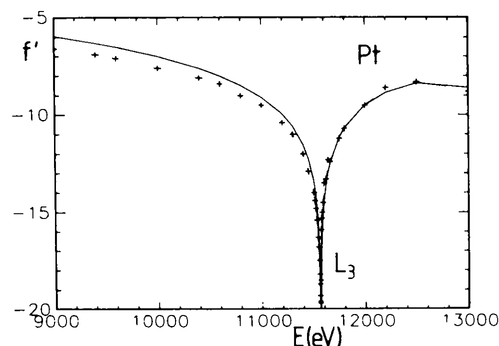


Fig. 14. Dispersive correction $f'(E)$ for metallic platinum determined by total reflection of X-rays (+). The data (——) are calculated according to Cromer & Liberman (1970).

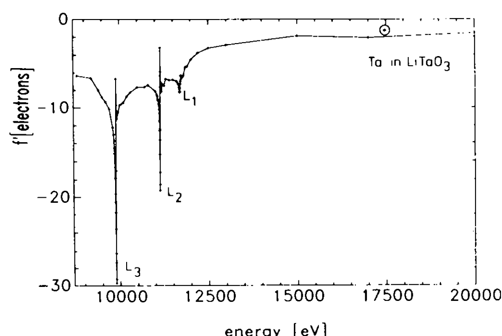


Fig. 15. Dispersive correction $f'(E)$ for Ta in $LiTaO_3$ determined by total reflection of X-rays (+).

Table 3. *Values of $f'(E)$ determined from X-ray reflection and values of $\mu/\rho$ measured in transmission at 77 K with the same energy calibration*

($a$) Metallic Ni

| Energy (eV) | $f'$ (electrons) | $\mu/\rho$ ($cm^2 g^{-1}$) |
|---|---|---|
| 7300.0 | −1.8 (6) | 65.0 |
| 7700.0 | −2.4 | 56.0 |
| 8000.0 | −2.9 | 51.2 |
| 8200.0 | −3.9 | 48.0 |
| 8225.0 | −4.1 | 47.5 |
| 8250.0 | −4.4 | 47.0 |
| 8265.0 | −4.6 | 47.0 |
| 8280.0 | −4.9 | 46.5 |
| 8290.0 | −5.2 | 46.0 |
| 8300.0 | −5.3 | 46.0 |
| 8305.0 | −5.5 | 46.0 |
| 8310.0 | −5.7 | 46.0 |
| 8315.0 | −6.0 | 46.0 |
| 8320.0 | −6.2 | 47.0 |
| 8325.0 | −6.7 | 48.0 |
| 8330.0 | −7.6 | 67.2 |
| 8332.0 | −7.8 | 125.5 |
| 8335.0 | −7.6 | 159.9 |
| 8337.0 | −7.7 | 178.5 |
| 8340.0 | −7.8 | 210.3 |
| 8342.0 | −8.1 | 242.1 |
| 8345.0 | −7.9 | 313.6 |
| 8347.0 | −7.4 | 345.4 |
| 8350.0 | −6.8 | 342.7 |
| 8355.0 | −6.3 | 356.0 |
| 8360.0 | −5.6 | 349.4 |
| 8370.0 | −5.6 | 332.1 |
| 8380.0 | −5.0 | 375.9 |
| 8400.0 | −4.8 | 330.0 |
| 8500.0 | −3.5 | 386.6 |
| 8600.0 | −2.7 | 320.0 |
| 8800.0 | −2.1 | 300.0 |
| 9000.0 | −1.7 | 281.0 |
| 9250.0 | −1.3 (6) | 260.0 |

($b$) Metallic Cu

| Energy (eV) | $f'$ (electrons) | $\mu/\rho$ ($cm^2 g^{-1}$) |
|---|---|---|
| 7600.0 | −1.6 (2) | 63.0 |
| 7800.0 | −1.7 | 58.0 |
| 8000.0 | −1.9 | 55.2 |
| 8200.0 | −2.1 | 54.0 |
| 8400.0 | −2.4 | 49.0 |
| 8600.0 | −2.8 | 44.0 |
| 8700.0 | −3.1 | 43.0 |
| 8800.0 | −3.5 | 41.0 |
| 8850.0 | −3.8 | 41.0 |
| 8900.0 | −4.3 | 41.0 |
| 8930.0 | −4.9 | 40.7 |
| 8960.0 | −5.8 | 40.7 |
| 8970.0 | −6.4 | 42.9 |
| 8975.0 | −6.9 | 45.1 |
| 8880.0 | −8.5 | 79.7 |
| 8982.0 | −7.8 | 163.3 |
| 8984.0 | −7.4 | 163.3 |
| 8986.0 | −7.7 | 170.0 |
| 8988.0 | −7.8 | 190.0 |
| 8990.0 | −7.9 | 221.3 |
| 8992.0 | −7.7 | 264.8 |
| 8994.0 | −7.1 | 302.7 |
| 8996.0 | −6.4 | 312.7 |
| 9000.0 | −6.3 | 286.0 |
| 9005.0 | −5.4 | 317.4 |
| 9010.0 | −5.3 | 284.9 |
| 9020.0 | −5.3 | 293.9 |
| 9030.0 | −4.4 | 309.5 |
| 9050.0 | −4.7 | 300.0 |
| 9070.0 | −4.5 | 325.0 |
| 9100.0 | −3.5 | 278.0 |

Table 3 (*cont.*)

($b$) Metallic Cu (*cont.*)

| Energy (eV) | $f'$ (electrons) | $\mu/\rho$ ($cm^2 g^{-1}$) |
|---|---|---|
| 9150.0 | −3.0 | 284.0 |
| 9200.0 | −3.1 | 290.0 |
| 9250.0 | −2.5 | 278.0 |
| 9300.0 | −2.4 | 297.0 |
| 9400.0 | −2.0 | 280.0 |
| 9500.0 | −1.7 | 265.0 |
| 9600.0 | −1.4 | 250.0 |
| 9700.0 | −1.3 | 243.0 |
| 9800.0 | −1.1 | 237.0 |
| 9900.0 | −1.0 | 232.0 |
| 10000.0 | −1.0 | 224.0 |
| 10500.0 | −0.5 | 199.0 |
| 11000.0 | −0.3 | 174.0 |
| 12000.0 | 0.0 (3) | 138.0 |
| 15000.0 | 0.2 | 75.1 |
| 17000.0 | 0.5 (4) | 53.2 |

($c$) Cu in CuO

| Energy (eV) | $f'$ (electrons) | $\mu/\rho$ ($cm^2 g^{-1}$) |
|---|---|---|
| 7800.0 | −1.7 (3) | 58.0 |
| 8000.0 | −1.9 | 55.2 |
| 8200.0 | −2.2 | 54.0 |
| 8400.0 | −2.4 | 49.0 |
| 8600.0 | −2.7 | 44.0 |
| 8800.0 | −3.5 | 41.0 |
| 8900.0 | −4.2 | 41.0 |
| 8950.0 | −5.2 | 40.7 |
| 8960.0 | −5.6 | 40.7 |
| 8970.0 | −6.1 | 40.7 |
| 8975.0 | −6.5 | 43.5 |
| 8980.0 | −7.0 | 51.8 |
| 8985.0 | −8.0 | 123.9 |
| 8990.0 | −8.5 | 193.3 |
| 8995.0 | −8.4 | 337.5 |
| 9000.0 | −6.3 | 379.1 |
| 9005.0 | −5.1 | 319.5 |
| 9010.0 | −5.2 | 297.3 |
| 9020.0 | −4.9 | 291.8 |
| 9030.0 | −5.2 | 268.2 |
| 9050.0 | −4.8 | 318.1 |
| 9100.0 | −3.9 | 298.4 |
| 9150.0 | −3.4 | 307.0 |
| 9200.0 | −3.0 | 293.0 |
| 9300.0 | −2.1 | 282.0 |
| 9400.0 | −1.9 | 274.0 |
| 9600.0 | −1.4 | 253.0 |
| 9800.0 | −1.0 | 240.0 |
| 10000.0 | −0.8 | 224.0 |
| 10200.0 | −0.5 (4) | 215.0 |
| 10500.0 | −0.2 | 199.0 |
| 12000.0 | 0.4 | 138.0 |
| 15000.0 | 0.3 | 75.1 |
| 20000.0 | 0.6 (7) | 33.8 |

($d$) Metallic Ta

| Energy (eV) | $f'$ (electrons) | $\mu/\rho$ ($cm^2 g^{-1}$) |
|---|---|---|
| 8998.0 | −6.6 (13) | 123.0 |
| 9098.0 | −6.8 | 120.0 |
| 9198.0 | −6.9 | 117.0 |
| 9298.0 | −7.3 | 113.0 |
| 9398.0 | −7.6 | 109.0 |
| 9498.0 | −8.1 | 107.0 |
| 9548.0 | −8.5 | 105.0 |
| 9598.0 | −8.8 | 103.0 |
| 9648.0 | −9.1 | 102.0 |
| 9698.0 | −10.4 | 100.0 |
| 9748.0 | −11.2 | 98.0 |
| 9798.0 | −12.4 | 97.0 |

Table 3 (*cont.*)

(*d*) Metallic Ta (*cont.*)

| Energy (eV) | $f'$ (electrons) | $\mu/\rho$ ($cm^2\ g^{-1}$) |
|---|---|---|
| 9838.0 | −14.4 | 96.5 |
| 9848.0 | −15.4 | 96.5 |
| 9853.0 | −16.4 | 96.5 |
| 9858.0 | −17.0 | 97.2 |
| 9863.0 | −18.0 | 98.0 |
| 9868.0 | −20.1 | 101.0 |
| 9870.0 | −21.4 | 104.0 |
| 9872.0 | −23.1 | 110.0 |
| 9874.0 | −25.4 | 137.0 |
| 9876.0 | −26.5 | 211.0 |
| 9878.0 | −24.7 | 333.0 |
| 9880.0 | −20.9 | 396.0 |
| 9883.0 | −15.7 | 335.0 |
| 9888.0 | −12.9 | 273.0 |
| 9893.0 | −12.6 | 255.0 |
| 9898.0 | −12.5 | 243.0 |
| 9908.0 | −12.8 | 236.0 |
| 9918.0 | −13.2 | 232.0 |
| 9928.0 | −13.1 | 235.0 |
| 9938.0 | −12.9 | 234.0 |
| 9958.0 | −12.5 | 232.0 |
| 9978.0 | −12.9 | 231.0 |
| 9998.0 | −12.1 | 232.0 |
| 10018.0 | −11.5 | 228.0 |
| 10038.0 | −12.1 | 227.0 |
| 10058.0 | −11.3 | 230.0 |
| 10078.0 | −11.1 | 225.0 |
| 10198.0 | −10.1 | 217.0 |
| 10498.0 | −8.7 | 197.0 |
| 10998.0 | −9.2 (13) | 180.0 |

(*e*) Ta in $LiTaO_3$

| Energy (eV) | $f'$ (electrons) | $\mu/\rho$ ($cm^2\ g^{-1}$) |
|---|---|---|
| 8798.0 | −6.3 (8) | 132.0 |
| 9198.0 | −6.6 | 116.0 |
| 9398.0 | −8.0 | 109.2 |
| 9498.0 | −8.8 (9) | 106.0 |
| 9598.0 | −9.3 | 103.0 |
| 9698.0 | −10.1 | 100.0 |
| 9798.0 | −12.2 | 97.0 |
| 9818.0 | −13.0 | 97.0 |
| 9838.0 | −14.6 | 97.0 |
| 9848.0 | −15.1 | 97.0 |
| 9858.0 | −16.6 | 100.0 |
| 9863.0 | −17.8 | 103.0 |
| 9868.0 | −19.6 | 111.7 |
| 9870.0 | −20.6 | 118.0 |
| 9872.0 | −21.8 | 128.0 |
| 9874.0 | −23.6 | 146.0 |
| 9876.0 | −26.3 | 181.0 |
| 9878.0 | −29.3 | 261.0 |
| 9879.0 | −29.7 | 326.0 |
| 9880.0 | −27.3 | 378.0 |
| 9883.0 | −17.0 | 393.0 |
| 9885.0 | −17.0 | 393.0 |
| 9888.0 | −6.7 | 302.0 |
| 9898.0 | −9.7 | 224.0 |
| 9908.0 | −11.2 | 225.0 |
| 9948.0 | −10.5 | 230.0 |
| 9998.0 | −9.7 | 229.0 |
| 10098.0 | −9.4 (10) | 223.0 |
| 10198.0 | −8.7 | 215.0 |
| 10298.0 | −8.3 | 209.0 |
| 10498.0 | −7.7 | 200.0 |
| 10698.0 | −7.6 | 192.0 |
| 10798.0 | −7.4 | 188.0 |
| 10998.0 | −8.1 | 180.0 |
| 11048.0 | −8.6 | 179.0 |
| 11058.0 | −8.8 | 179.0 |
| 11068.0 | −9.1 | 178.0 |

Table 3 (*cont.*)

(*e*) Ta in $LiTaO_3$ (*cont.*)

| Energy (eV) | $f'$ (electrons) | $\mu/\rho$ ($cm^2\ g^{-1}$) |
|---|---|---|
| 11078.0 | −9.1 | 178.0 |
| 11088.0 | −9.2 | 178.0 |
| 11098.0 | −9.6 | 177.0 |
| 11103.0 | −9.8 | 177.0 |
| 11108.0 | −10.2 | 177.0 |
| 11113.0 | −10.6 | 178.0 |
| 11118.0 | −11.6 | 178.0 |
| 11123.0 | −12.8 | 179.0 |
| 11126.0 | −13.8 | 182.0 |
| 11129.0 | −15.7 | 187.0 |
| 11132.0 | −18.6 | 218.0 |
| 11134.0 | −19.2 | 316.0 |
| 11135.0 | −15.3 | 375.0 |
| 11136.0 | −11.4 | 410.0 |
| 11138.0 | −7.4 (10) | 401.0 |
| 11140.0 | −6.0 | 369.0 |
| 11143.0 | −3.4 | 327.0 |
| 11148.0 | −6.0 | 254.0 |
| 11158.0 | −7.8 | 236.0 |
| 11173.0 | −8.2 (11) | 238.0 |
| 11198.0 | −7.3 | 248.0 |
| 11248.0 | −7.5 | 241.0 |
| 11298.0 | −6.7 | 238.0 |
| 11398.0 | −6.8 | 234.0 |
| 11498.0 | −6.8 | 227.0 |
| 11598.0 | −7.0 | 221.0 |
| 11648.0 | −7.3 | 219.0 |
| 11668.0 | −7.7 | 220.0 |
| 11678.0 | −7.9 | 223.0 |
| 11683.0 | −8.2 | 230.0 |
| 11688.0 | −8.3 | 236.0 |
| 11693.0 | −8.2 | 248.0 |
| 11698.0 | −7.7 | 263.0 |
| 11703.0 | −7.3 | 261.0 |
| 11708.0 | −7.0 | 261.0 |
| 11718.0 | −6.3 | 262.0 |
| 11728.0 | −6.3 | 252.0 |
| 11748.0 | −6.6 | 250.0 |
| 11798.0 | −6.3 | 251.0 |
| 11848.0 | −5.4 | 248.0 |
| 11898.0 | −5.3 | 245.0 |
| 11998.0 | −4.6 | 240.0 |
| 12198.0 | −3.8 | 231.0 |
| 12498.0 | −3.3 | 218.0 |
| 12998.0 | −2.9 (12) | 199.0 |
| 14998.0 | −1.9 (14) | 134.0 |
| 16998.0 | −2.1 | 95.9 |
| 19998.0 | −1.6 (18) | 62.2 |

(*f*) Metallic Pt

| Energy (eV) | $f'$ (electrons) | $\mu/\rho$ ($cm^2\ g^{-1}$) |
|---|---|---|
| 8999.0 | −6.6 (4) | 149.0 |
| 9399.0 | −6.9 | 134.0 |
| 9599.0 | −7.1 | 127.0 |
| 9999.0 | −7.6 | 114.0 |
| 10399.0 | −8.1 | 103.0 |
| 10599.0 | −8.4 | 98.0 |
| 10799.0 | −9.0 (5) | 93.0 |
| 10999.0 | −9.5 | 89.0 |
| 11199.0 | −10.4 | 84.5 |
| 11299.0 | −11.0 | 82.5 |
| 11399.0 | −12.0 | 80.5 |
| 11449.0 | −12.9 | 79.0 |
| 11499.0 | −14.0 | 78.5 |
| 11509.0 | −14.4 | 78.5 |
| 11519.0 | −14.8 | 78.5 |
| 11529.0 | −15.4 | 78.5 |
| 11539.0 | −16.3 | 79.0 |
| 11544.0 | −16.8 | 80.5 |
| 11549.0 | −17.5 | 84.5 |

Table 3 (*cont.*)

(*f*) Metallic Pt (*cont.*)

| Energy (eV) | $f'$ (electrons) | $\mu/\rho$ ($cm^2\,g^{-1}$) |
|---|---|---|
| 11553.0 | −18.2 | 91.0 |
| 11555.0 | −18.7 | 97.0 |
| 11557.0 | −19.3 | 107.5 |
| 11559.0 | −19.6 | 131.0 |
| 11563.0 | −19.7 | 220.0 |
| 11565.0 | −18.5 | 218.0 |
| 11569.0 | −15.9 | 200.0 |
| 11574.0 | −15.3 | 193.0 |
| 11579.0 | −15.0 | 197.0 |
| 11589.0 | −14.5 | 198.0 |
| 11599.0 | −13.5 | 196.0 |
| 11619.0 | −13.3 | 199.0 |
| 11639.0 | −12.3 | 194.0 |
| 11659.0 | −12.4 | 195.0 |
| 11749.0 | −11.2 | 193.0 |
| 11799.0 | −10.7 | 190.0 |
| 11999.0 | −9.5 | 183.0 |
| 12199.0 | −8.6 | 176.0 |
| 12499.0 | −8.3 | 164.0 |
| 12999.0 | −8.8 (5) | 147.0 |

(*g*) Metallic Au

| Energy (eV) | $f'$ (electrons) | $\mu/\rho$ ($cm^2\,g^{-1}$) |
|---|---|---|
| 7000.0 | −4.4 (3) | 296.0 |
| 7200.0 | −4.4 | 274.0 |
| 7400.0 | −4.5 | 257.0 |
| 7600.0 | −4.6 | 240.0 |
| 8000.0 | −4.8 (4) | 211.0 |
| 8200.0 | −5.0 | 198.0 |
| 8400.0 | −5.2 | 187.0 |
| 8600.0 | −5.2 | 175.0 |
| 8800.0 | −5.3 | 165.0 |
| 9200.0 | −5.6 | 149.0 |
| 9400.0 | −5.9 | 140.0 |
| 9600.0 | −6.2 | 132.0 |
| 10000.0 | −6.7 | 118.0 |
| 10200.0 | −6.7 (5) | 112.0 |
| 10400.0 | −6.7 | 106.0 |
| 10508.0 | −7.1 | 103.0 |
| 10600.0 | −7.0 | 101.0 |
| 10808.0 | −7.6 | 96.0 |
| 11008.0 | −8.0 | 91.0 |
| 11208.0 | −8.5 | 87.0 |
| 11408.0 | −9.3 | 84.0 |
| 11501.0 | −9.5 | 83.0 |
| 11608.0 | −10.1 | 81.0 |
| 11708.0 | −11.0 | 79.0 |
| 11808.0 | −12.0 | 77.0 |
| 11888.0 | −14.0 | 77.5 |
| 11898.0 | −15.0 | 78.5 |
| 11918.0 | −18.4 | 98.5 |
| 11923.0 | −18.7 | 151.0 |
| 11926.0 | −17.6 | 161.0 |
| 11928.0 | −17.3 | 162.0 |
| 11930.0 | −17.2 | 162.0 |
| 11933.0 | −16.9 | 169.0 |
| 11936.0 | −17.0 | 173.0 |
| 11938.0 | −16.3 | 174.0 |
| 11940.0 | −16.2 | 175.0 |
| 11943.0 | −16.2 | 181.0 |
| 11946.0 | −15.8 | 190.0 |
| 11948.0 | −15.3 | 192.0 |
| 11953.0 | −14.8 | 184.0 |
| 11958.0 | −14.6 | 181.0 |
| 11963.0 | −14.8 | 182.0 |
| 11968.0 | −14.4 | 189.0 |
| 11971.0 | −13.7 | 188.4 |
| 11981.0 | −12.8 | 186.0 |
| 11991.0 | −12.3 | 182.0 |

Table 3 (*cont.*)

(*g*) Metallic Au (*cont.*)

| Energy (eV) | $f'$ (electrons) | $\mu/\rho$ ($cm^2\,g^{-1}$) |
|---|---|---|
| 12001.0 | −12.6 | 183.0 |
| 12108.0 | −11.1 | 179.0 |
| 12208.0 | −10.4 | 175.0 |
| 12408.0 | −9.1 (6) | 169.0 |
| 12608.0 | −8.5 | 160.0 |
| 12808.0 | −8.2 | 152.0 |
| 13008.0 | −7.9 (6) | 145.0 |
| 13101.0 | −7.8 | 143.0 |
| 13151.0 | −7.8 | 141.0 |
| 13201.0 | −7.9 | 140.0 |
| 13251.0 | −7.9 | 139.0 |
| 13301.0 | −7.9 | 138.0 |
| 13351.0 | −8.0 | 137.0 |
| 13401.0 | −8.2 | 135.0 |
| 13451.0 | −8.3 | 134.0 |
| 13501.0 | −8.5 | 133.0 |
| 13551.0 | −8.5 | 131.0 |
| 13601.0 | −8.7 | 130.0 |
| 13621.0 | −9.0 | 129.0 |
| 13641.0 | −9.2 | 129.0 |
| 13661.0 | −9.3 | 128.0 |
| 13681.0 | −9.6 | 127.5 |
| 13701.0 | −10.1 | 128.0 |
| 13711.0 | −10.4 | 128.0 |
| 13716.0 | −10.7 | 128.0 |
| 13721.0 | −11.0 | 128.5 |
| 13726.0 | −11.4 | 129.3 |
| 13731.0 | −11.9 | 133.0 |
| 13736.0 | −12.3 | 148.9 |
| 13741.0 | −12.0 | 159.3 |
| 13746.0 | −11.7 | 168.9 |
| 13751.0 | −11.3 | 170.8 |
| 13756.0 | −11.2 | 173.9 |
| 13761.0 | −10.9 | 180.3 |
| 13766.0 | −10.3 | 178.3 |
| 13771.0 | −10.3 | 176.5 |
| 13781.0 | −10.4 | 180.2 |
| 13791.0 | −9.9 | 179.3 |
| 13801.0 | −9.7 | 176.5 |
| 13821.0 | −9.6 | 178.0 |
| 13841.0 | −9.3 | 176.0 |
| 13861.0 | −9.0 | 174.0 |
| 13881.0 | −9.0 | 174.5 |
| 13901.0 | −9.0 | 174.0 |
| 13951.0 | −8.7 | 172.0 |
| 14001.0 | −8.7 | 170.0 |
| 14051.0 | −8.4 | 168.0 |
| 14101.0 | −8.3 | 166.0 |
| 14201.0 | −8.2 | 162.0 |
| 14251.0 | −8.1 | 161.0 |
| 14301.0 | −8.3 | 158.8 |
| 14321.0 | −8.6 | 158.1 |
| 14331.0 | −8.7 | 158.0 |
| 14336.0 | −8.8 | 158.4 |
| 14341.0 | −9.0 | 158.8 |
| 14346.0 | −9.3 | 160.0 |
| 14351.0 | −9.4 | 163.0 |
| 14356.0 | −9.5 | 170.0 |
| 14361.0 | −9.3 | 179.4 |
| 14366.0 | −8.6 | 189.1 |
| 14381.0 | −8.7 | 185.2 |
| 14391.0 | −7.9 (6) | 190.1 |
| 14401.0 | −7.7 | 187.5 |
| 14421.0 | −7.6 (7) | 187.0 |
| 14451.0 | −7.4 | 185.0 |
| 14501.0 | −7.0 | 184.0 |
| 15001.0 | −5.2 | 168.0 |
| 16001.0 | −3.9 | 140.0 |
| 18001.0 | −2.2 (8) | 105.0 |
| 20001.0 | −1.4 | 78.2 |
| 22001.0 | −1.2 | 63.0 |
| 25001.0 | −0.8 (11) | 43.4 |
| 27001.0 | −0.8 | 36.0 |

Table 3. Fig. 16 shows the dispersive correction $f'(E)$ for metallic tantalum determined by X-ray reflection and by the Kramers-Kronig relation (Dreier *et al.*, 1984). The agreement is very satisfactory. Due to the strong absorption (white line) at the Ta $L_3$ edge, the data calculated according to Cromer & Liberman (1970) do not agree with our data in the vicinity of the edge. Here the experimental data are superior in quality to the calculated ones.

This example shows an interesting application of X-ray reflection. The density of thin films can strongly depend on the method of deposition. X-ray reflection is an easy nondestructive method to determine this value with great precision, even in layers as thin as 100 Å.

(v) *Metallic* Cu [*sample* (v) *in Table* 1]

Reflectivity measurements were made in the energy range from 7.6 to 17 keV. The density of the Cu film was assumed to be 8.96 g cm$^{-3}$ (Landolt-Börnstein, 1971). The thin oxide layer of 35 Å observed in X-ray absorption is best described by an additional contribution to the roughness. The data were fitted with models 1 and 2. Fig. 17 shows $f'(E)$ and $\mu/\rho$ in the vicinity of the $K$ edge. The values of $f'(E)$ agree well with those determined by Bonse & Hartmann-Lotsch (1986) by interferometry. The data calculated according to Cromer & Liberman (1970) do not agree with the experimental values at and above the Cu $K$ edge. The edge structure and the EXAFS are not taken into account in the calculation. All the values of $f'(E)$ measured on Cu by total reflection are listed in Table 3. The error in $f'(E)$ is mainly due to errors in $\theta_1$. It is ±0.3 electrons between 7.6 and 13 keV and increases to ±0.5 electrons at 17 keV. Model 1 gave a surface roughness $\sigma_1 = 18(1)$ Å or 42(2) Å FWHM. Model 2 describing the surface roughness (including the oxide) by a surface layer gave a thickness of 34(2) Å for that layer and a density of 6(1) g cm$^{-3}$. These results agree well with the thickness of the oxide layer determined by absorption. From the period of the oscillations in $R$ a thickness of the Cu layer of 970(10) Å was found. The Cu/Ti interface has a roughness of $\sigma_2 = 15(2)$ Å.

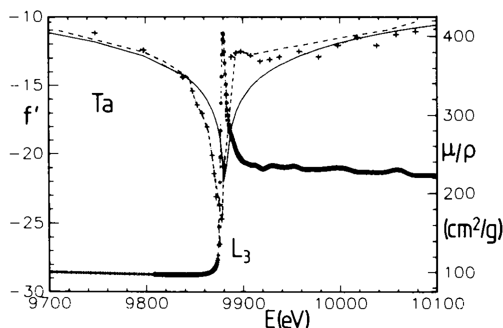


Fig. 16. Dispersive correction $f'(E)$ for metallic Ta determined by X-ray reflection (+ · · · +), by Kramers-Kronig (– · – · –) (Dreier *et al.*, 1984) and by Cromer & Liberman (1970) (——). The mass absorption $\mu/\rho$ measured by X-ray absorption in a foil at 77 K is also shown (*).

(vi) CuO [*sample* (vi) *in Table* 1]

Reflectivity data were collected between 7.800 and 20.000 keV. They were fitted according to model 2. The density of the CuO was determined from total reflection using $f'(E)$ values of metallic Cu far below the $K$ edge. A value of 5.84 g cm$^{-3}$ was found which is about 9% smaller than the bulk density of CuO, which lies between 6.3 and 6.57 g cm$^{-3}$ (Landolt-Börnstein, 1971). It is not unusual that sputtered films have reduced density compared to the bulk density. The dispersive correction $f'(E)$ and the absorption coefficient $\mu/\rho$ for CuO are given in Table 3. The $K$ edge of Cu in CuO is higher in energy by 4.5 eV compared to that in metallic copper (Table 3). The same shift is also observed in the values of $f'(E)$ below the edge (Fig. 18). This means that $f'(E)$ values below absorption edges can be transferred from one compound to another (with the same absorber) provided the shift in edge position is taken care of. Values of $f'(E)$ above absorption edges are not transferable due to different EXAFS. A similar behavior was also

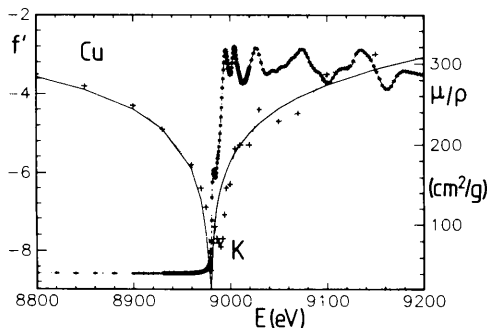


Fig. 17. Dispersive correction $f'(E)$ from total reflection (+ · · · +) and by Cromer & Liberman (1970) (——) and absorption coefficient $\mu/\rho$ (*) for metallic Cu near the $K$-absorption edge.

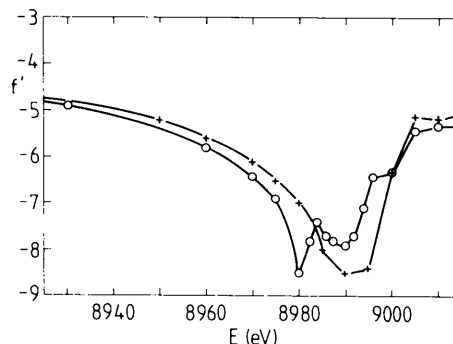


Fig. 18. Dispersive correction $f'(E)$ of Cu in Cu metal (O) and in CuO (+). The edge positions differ in energy by 4.5 eV.

observed for Ta and $LiTaO_3$, although in this case the energy shift between the edges was only 1 eV.

(vii) *Metallic* Ni [*sample* (vii) *in Table* 1]

Reflection data were collected between 7.300 and 9.250 keV. The density of bulk Ni is 8.912 g cm$^{-3}$ (Landolt-Börnstein, 1971). With this value the correction $f'(E)$ turned out to be systematically higher by 0.7 electrons compared to those determined interferometrically by Bonse & Hartmann-Lotsch (1986). With a density of 8.69 g cm$^{-3}$ our data fit very well with those of Bonse & Hartmann-Lotsch. The dispersive correction $f'(E)$ and the absorption coefficient $\mu/\rho$ near the Ni $K$ edge are shown in Fig. 19. As in the case of Cu and Ta, the data calculated according to Cromer & Liberman (1970) do not agree with the experimental values at and above the Ni $K$ edge. The complete set of data is listed in Table 3.

In summary, the dispersive correction $f'(E)$ to the atomic form factor has been determined for a number of elements and compounds from X-ray reflectivity. The precision is comparable to that obtained by interferometry. The data calculated by Cromer & Liberman (1970) agree well with our data far from absorption edges. At the edges there are substantial differences that are due to the fact that the Cromer & Liberman calculations do not take into account the structure of the edge, their chemical shift and the EXAFS structure above the edges. The data $f'(E)$ as well as the absorption coefficient $\mu/\rho$ are given in Table 3 for Ni, Cu, CuO, Ta, $LiTaO_3$, Pt and Au. It is shown that reflectivity measurements can be used to determine the density of a film on a substrate, once $f'(E)$ is known. The method allows one to obtain, in addition, the thickness of the film and the interface roughness.

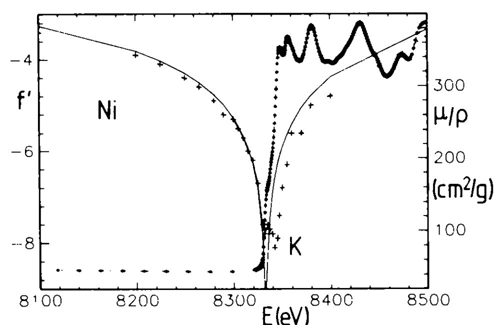


Fig. 19. Dispersive correction $f'(E)$ for metallic Ni determined by X-ray reflection (+ · · · +) and by Cromer & Liberman (1970) (——). Also shown is the mass absorption $\mu/\rho$ (*) measured by X-ray absorption at 77 K.

## References


Beckmann, P. & Spizzichino, A. (1963). *The Scattering of Electromagnetic Waves from Rough Surfaces.* New York: Pergamon.

Begum, R., Hart, M., Lea, K. R. & Siddons, D. P. (1986). *Acta Cryst.* **A42**, 456-464.

Bonse, U. & Hart, M. (1965). *Appl. Phys. Lett.* **7**, 238-240.

Bonse, U. & Hart, M. (1966). *Z. Phys.* **189**, 151-162.

Bonse, U. & Hartmann-Lotsch, I. (1986). *Nucl. Instrum. Methods*, **222**, 185-188.

Born, M. & Wolf, E. (1965). *Principles of Optics.* New York: Pergamon.

Burr, A. (1974). In *Handbook of Spectroscopy*, Vol. I, edited by J. W. Robinson, pp. 23-27. Cleveland, Ohio: CRC Press.

Compton, A. H. & Allison, S. K. (1935). *X-rays in Theory and Experiment.* Princeton, NJ: D. van Nostrand.

Cromer, D. T. (1983). *J. Appl. Cryst.* **16**, 437.

Cromer, D. T. & Liberman, D. (1970). *J. Chem. Phys.* **53**, 1891-1898.

Dreier, P., Rabe, P., Malzfeldt, W. & Niemann, W. (1984). *J. Phys. C*, **17**, 3123-3136.

Eisenberger, P. & Marra, W. C. (1981). *Phys. Rev. Lett.* **46**, 1081-1084.

Fukamachi, T., Hosoya, S., Kawamura, T., Hunter, S. & Nakano, Y. (1978). *Jpn. J. Appl. Phys.* **S17**, 326-328.

Jackson, J. D. (1975). *Classical Electrodynamics.* New York: J. Wiley.

James, R. W. (1967). *The Optical Principles of the Diffraction of X-rays.* Cornell Univ. Press.

Kawamura, T. & Fukamachi, T. (1978). *Jpn. J. Appl. Phys.* **S17**, 224-226.

Kiessig, H. (1931). *Ann. Phys. (Leipzig)*, **10**, 715-768, 769-788.

Krolzig, A., Materlik, G., Swars, M. & Zegenhagen, J. (1984). *Nucl. Instrum. Methods*, **219**, 430-434.

Landolt-Börnstein (1971). *Neue Serie*, Vols. 6 and 7, edited by K. H. Hellwege. Berlin: Springer.

Nevot, L. & Croce, P. (1980). *Rev. Phys. Appl.* **15**, 761-779.

Parratt, L. G. & Hempstead, C. F. (1954). *Phys. Rev.* **94**, 1593-1600.

Siddons, D. P. & Hart, M. (1983). In *EXAFS and Near-Edge Structures*, edited by A. Bianconi, L. Incoccia & S. Stipcich, pp. 373-375. Berlin: Springer-Verlag.

Sinha, S. K., Sirota, E. B., Garoff, S. & Stanley, H. B. (1988). *Phys. Rev. B*, **38**, 2297-2311.

Storb, C., Dedek, U., Lengeler, B., Weber, W. & Schuster, M. (1991). *Nucl. Instrum. Methods Phys. Res.* **A306**, 544-548.

Stuhrmann, H. B. (1981). *Q. Rev. Biophys.* **14**, 433-462.

Veigele, W. J. (1974). In *Handbook of Spectroscopy*, Vol. I, edited by J. W. Robinson, pp. 28-154. Cleveland, Ohio: CRC Press.

Vineyard, G. H. (1982). *Phys. Rev. B*, **26**, 4146-4159.

Weber, W. & Lengeler, B. (1992). Submitted to *Phys. Rev.*